Heavily boron-doped diamond grown on scalable heteroepitaxial quasi-substrates
A promising single crystal material for electrochemical sensing applications

Liu, Zhichao; Baluchová, Simona; Sartori, André F.; Li, Ziyu; Gonzalez-Garcia, Yaiza; Schreck, Matthias; Buijnsters, Josephus G.

Important note
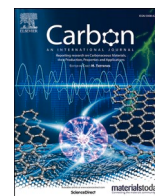To cite this publication, please use the final published version (if applicable).
Please check the document version above.

Contents lists available at ScienceDirect

Carbon

Heavily boron-doped diamond grown on scalable heteroepitaxial quasi-substrates: A promising single crystal material for electrochemical sensing applications

Zhichao Liu [a], Simona Baluchová [a], André F. Sartori [a], Ziyu Li [b], Yaiza Gonzalez-Garcia [b], Matthias Schreck [c], Josephus G. Buijnsters [a,*]

[a] *Department of Precision and Microsystems Engineering, Delft University of Technology, Mekelweg 2, 2628 CD, Delft, the Netherlands*
[b] *Department of Materials Science and Engineering, Delft University of Technology, Mekelweg 2, 2628 CD, Delft, the Netherlands*
[c] *Experimentalphysik IV, Institut für Physik, University of Augsburg, Universitätsstraße 1, 86135, Augsburg, Germany*

ARTICLE INFO

ABSTRACT

In this work, three distinct heteroepitaxial single-crystal boron-doped diamond (SC-BDD) electrodes were fabricated and subjected to detailed surface analysis and electrochemical characterization. Specifically, the heteroepitaxy approach allowed to synthesize large-area (1 cm^2) and heavily-doped (100)-oriented SC-BDD electrodes. Their single-crystal nature and crystal orientation were confirmed by X-ray diffraction, while scanning electron and atomic force microscopies revealed marked variations in surface morphology resulting from their growth on respective on-axis and off-axis substrates. Further, absence of sp^2 impurities along with heavy boron doping ($>10^{21}$ cm^{-3}) was demonstrated by Raman spectroscopy and Mott-Schottky analysis, respectively. Cyclic voltammetry (CV) in a 0.1 M KNO$_3$ solution revealed wide potential windows ($\sim$3.3 V) and low double-layer capacitance ($<$4 μF cm^{-2}) of the SC-BDD electrodes. Their highly conductive, 'metal-like' nature was confirmed by CV with [Ru(NH$_3$)$_6$]$^{3+/2+}$ probe manifesting near-reversible redox response with ΔE_p approaching 0.059 V. The same probe was used to record scanning electrochemical micrographs, which clearly demonstrated homogeneously distributed electrochemical activity of the heteroepitaxial SC-BDD electrodes. Minor differences in their electrochemical performance, presumably resulting from the somewhat different morphological features, were only unveiled during CV with surface sensitive compounds [Fe(CN)$_6$]$^{3-/4-}$ and dopamine. The latter was also used to show the possibility of applying herein developed heteroepitaxial SC-BDD electrodes for electrochemical sensing, whereas experiments with anthraquinone-2,6-disulfonate revealed their enhanced resistance to fouling. All in all, heteroepitaxial SC-BDD represents a highly attractive electrode material which can, owing to the fabrication strategy, easily overcome size limitation, currently preventing broader use of single crystal diamond electrodes in electrochemical applications.

1. Introduction

Electrically conductive boron-doped diamond (BDD) is a remarkably versatile electrode material [1], which has been extensively employed in numerous electrochemical applications, such as electroanalysis and (bio)sensors development [2,3], pollutant degradation and waste-water treatment [4–7], electro-organic synthesis [8], electrocatalysis [9], and electrochemical energy storage [10] as well as in "non-electrochemical" research fields, including biomedicine and neuroscience [11,12]. The unprecedented popularity of BDD, particularly in electroanalysis, results

from a large range of outstanding characteristics, distinguishing BDD from other commonly employed carbonaceous and metallic electrodes. These properties include exceptional chemical and mechanical stability, resistance towards corrosion and (bio)fouling, wide working potential window, possibility of *in-situ* electrochemical activation, dopant-controlled adjustable conductivity, low noise and background current, and biocompatibility [1,2].

Notably, a vast majority of BDD electrodes produced and employed for sensor development are of polycrystalline nature with diamond grains composed of various crystal facets and with related grain

---

boundaries. The polycrystalline BDD surface is thus inhomogeneous, and the following aspects must be considered carefully:

i) The incorporation efficiency of boron dopant into the diamond layer is strongly influenced by the crystallographic orientation of the growth facets; the uptake decreases in the following order: (111) > (110) > (100) [13,14]. This naturally results in heterogeneous doping and distribution of boron carriers within the BDD layer, creating less or more conductive domains [15], influencing the diffusion field and kinetics of electron transfer (ET) reactions.

ii) As-prepared BDD electrodes are hydrogen (H)-terminated with hydrophobic, non-polar surfaces, which can be, however, converted into oxygen (O)-terminated, and thus hydrophilic and polar surfaces [16,17], by suitable (*in-situ*) pre-treatment procedures. The conversion from H- to O-termination is, though, also affected by the crystallographic orientation of the diamond grains as the propensity towards oxidation differs between the individual grain planes: (110) facet was identified to be more prone to oxidation than (100) and (111) facets [18].

iii) Non-diamond (sp^2) carbon impurity typically resides in the grain boundary phases [1,17]. The presence of sp^2 carbon impurities, more pronounced in heavily doped BDD electrodes [19], is electrochemically indicated by narrowed potential windows, increased background currents and higher proclivity towards adsorption [17,20], which are all detrimental phenomena in electroanalysis.

The polycrystalline character of BDD thus significantly affects the electrochemical properties, and consequently ET kinetics at the electrode–electrolyte interface. However, to study the inherent electrochemical features of BDD, the above-mentioned factors contributing to its heterogeneity must be eliminated. This can be achieved by preparing and using a single-crystal (SC) form of conductive diamond with a well-defined surface composition and orientation. Until now, only a few studies have utilised and clarified the performance of high-quality SC-BDD electrodes, while most attention has been paid to the crystallographic orientations which naturally occur in polycrystalline diamond, *i.e.*, (100) and (111) [14,21–24].

Substantially faster ET kinetics for $[Ru(NH_3)_6]^{3+/2+}$ and $[Fe(CN)_6]^{3-/4-}$ redox markers have been observed on (111) facet compared to (100)-oriented SC-BDD [22]. This was explained by the fact that both SC-BDD electrodes were deposited using the same B/C ratio, but due to the differences in boron uptake efficiency of (100) and (111) surfaces, the resulting boron concentration ([B]) in the diamond films varied by one order of magnitude ([B] of 2×10^{18} cm^{-3} for (100) *vs.* 2×10^{19} cm^{-3} for (111)). Such variation in doping level, and thus conductivity, naturally manifested in the obtained electrochemical responses for tested redox couples. In another work, Pleskov et al. concluded that identically doped (100) and (111)-oriented SC-BDD electrodes ([B] of 6×10^{18} cm^{-3}) provided comparable ET kinetics of $[Ru(NH_3)_6]^{3+/2+}$ and $[Fe(CN)_6]^{3-/4-}$, unaffected by the crystallographic orientation [14]. However, Ivandini et al. [23] studied (100) and (111)-faceted SC-BDD electrodes of higher boron doping (both facets contained [B] $\sim 4 \times 10^{20}$ cm^{-3}) and, despite the similar doping level, more sluggish ET kinetics and smaller peak currents of $[Ru(NH_3)_6]^{3+/2+}$ and $[Fe(CN)_6]^{3-/4-}$ couples were recorded on (100) surface in comparison with the (111) crystal. In this case, crystallographic orientation, particularly the difference in magnitude in band bending and the thickness of the space charge layer, was identified as the main factor responsible for different electrochemical behaviour of tested (100) and (111) SC-BDD electrodes [23]. Besides, less "conventional" monocrystalline diamond facets such as (113), (115) and (118) have been recently prepared and used as a substrate for SC-BDD deposition [25,26]; among them, the highest boron incorporation efficiency was confirmed for the (113) plane [25].

It is important to point out that all SC-BDD electrodes examined in these reports were homoepitaxially grown on synthetic single-crystal diamond substrates with a size of few mm^2. Such limitation in the crystal size presents the major drawback of homoepitaxial growth and restricts the use of SC-BDD for electrochemical sensing and pollutant degradation; particularly for the latter application satisfactorily high surface area is essential. One promising approach to effectively tackle the size issue is to employ heteroepitaxy, in which epitaxial nucleation and growth of diamond is controlled upon the surface of a different crystalline material [27]. Consequently, the selection of optimal substrate and suitable nucleation method is crucial for successful fabrication of high-quality heteroepitaxial diamond layers [27,28]. The combination of iridium-based materials and bias-enhanced nucleation technique has been recognized as the most suitable for diamond heteroepitaxy and has resulted in the preparation of the free-standing monocrystalline diamond wafer with a diameter of 9.2 cm by Schreck's group [28]. The same group investigated boron doping of heteroepitaxial SC diamond films and evaluated their composition, structure and functionality for the realization of competitive electronic devices and sensors [29,30].

In the present study, the diamond heteroepitaxy approach was applied for the first time to synthesize large-area (1 cm^2) and heavily-doped ([B] > 10^{21} cm^{-3}) (100)-oriented SC-BDD electrodes. BDD layers were grown on both on-axis and off-axis quasi-substrates to study the impact of a small off-cut angle. A total of three SC-BDD samples were prepared differing in their surface morphology. Scanning electron microscopy (SEM), atomic force microscopy (AFM) and two-dimensional X-ray diffraction (2D XRD) were used for surface and crystallographic analysis. The electrochemical properties of the BDD layers grown on heteroepitaxial diamond quasi-substrates were investigated and compared to the performance of conventional poly-BDD. Cyclic voltammetry (CV) was performed in solutions of a supporting electrolyte (0.1 M KNO$_3$) and two redox probes ($[Ru(NH_3)_6]^{3+/2+}$ and $[Fe(CN)_6]^{3-/4-}$) to assess important electrochemical characteristics such as the width of the potential window, double-layer capacitance (C_{dl}) and peak-to-peak separation (ΔE_p) values reflecting the rate of ET kinetics. Besides, scanning electrochemical microscopy (SECM) was employed to probe the distribution of the electrochemical activity of the SC-BDD and poly-BDD surfaces. Finally, the heteroepitaxial SC-BDD electrodes were subjected to voltammetric experiments with more complex organic molecules, namely dopamine to evaluate their perspective for sensing applications, and anthraquinone-2,6-disulfonate (AQDS) to demonstrate their anti-fouling property.

2. Experimental

2.1. Fabrication of heteroepitaxial SC-BDD layers

The preparation of the substrate used for heteroepitaxial diamond growth, Ir/yttria-stabilized zirconia (YSZ)/Si(100), is briefly described in Supplementary material and has also been reported in Ref. [29]. Fig. 1 illustrates the preparation of the three heteroepitaxial SC-BDD electrodes using the multi-layered stack (Fig. 1(a)). Prior to BDD growth, the YSZ/Si(100) was etched away, the iridium layer was removed by mechanical polishing, and the wafer (4 inch) was sliced by an IR laser into 1×1 cm^2 pieces which resulted in free-standing single crystal diamond samples, as depicted in Fig. 1(b). Then, the heteroepitaxial diamond quasi-substrates were exposed to the following processing (Fig. 1(c)): For samples A and B, 4° off-axis was preserved and the top (growth) side of sample A was polished (the back side of both samples was already polished due to removal of iridium layer), while sample C was polished on both sides to eliminate the off-axis angle. This also resulted in a lower thickness of sample C than samples A and B (0.26 mm vs. 1.37–1.29 mm, respectively). Finally, reactive ion etching was applied to remove polishing-induced crystal damage that is known to cause the nucleation of dislocations in subsequent homoepitaxial growth steps.

As further shown in Fig. 1(d), the BDD layers were grown either on
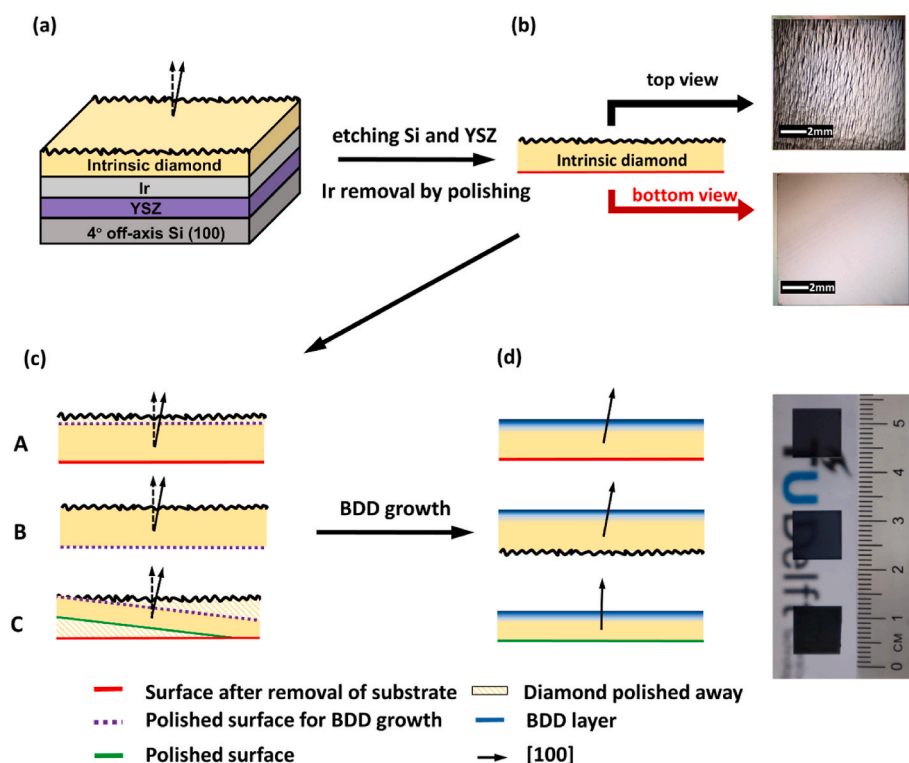
Fig. 1. Schematic displaying the fabrication of the three heteroepitaxial SC-BDD electrodes. **(a)** The layered stack was subjected to etching to remove YSZ and Si(100) and then to polishing to remove the Ir layer, which resulted in **(b)** free-standing, hetero-epitaxially grown intrinsic diamond with 4° off-axis (100) plane, whose top and bottom views were visualized by a digital microscope. **(c)** The intrinsic diamond was further processed: For samples A and B, 4° off-axis was preserved, and the top (growth) side of sample A was polished (the back side of both samples was already polished due to Ir layer removal), while sample C was polished on both sides to eliminate the off-axis angle. **(d)** BDD layers were grown either on the polished top side (samples A and C) or the back side (sample B; flipped by 180° prior to BDD growth step) of the heteroepitaxial diamond quasi-substrate. Prepared (100)-faceted SC-BDD electrodes (1 cm²) are shown in the picture (ruler with cm-scale). (A colour version of this figure can be viewed online.)

the polished top side (samples A and C) or the back side (sample B) of the heteroepitaxial (100) diamond quasi-substrate. The main difference between the top and back side of the heteroepitaxial diamond is the dislocation density, being higher on the back side (originally interfacing the iridium layer) [31,32]. To test if the increased amount of dislocations impact substantially the final electrode performance, both sides were used for the BDD growth carried out under following conditions: 1.1 kW microwave power, 750–850 °C substrate temperature, 50 mbar pressure and 4 h growth duration, while the gas mixture consisting of CH_4 and trimethylboron diluted in H_2 was carefully controlled to achieve heavy boron doping of $[B] > 10^{21}$ atoms cm^{-3} (detailed description of the BDD growth process is provided in Supplementary material). As-produced SC-BDD electrodes will be labelled as SC-BDD A, SC-BDD B and SC-BDD C, respectively, from here onwards.

As shown in Fig. 1, heteroepitaxial SC-BDD electrodes with dimensions of 1×1 cm² were prepared which already represents a significant improvement in size, compared to previously reported studies utilizing homoepitaxially grown SC-BDD (with an area of a few mm²). This size of the electrodes was selected purely for practical reasons (fitting into a home-built voltammetric cell), however, herein reported heteroepitaxy approach allows scaling up to even larger areas [28] if required by intended applications, *e.g.*, in waste water treatment, electrosynthesis and electrocatalysis.

2.2. Surface and crystallographic characterization

The surface morphology of the heteroepitaxial SC-BDD layers and poly-BDD was visualized by a scanning electron microscope JEOL JSM6500F in a secondary electron imaging mode operated at 15 keV. Surface roughness was determined from AFM measurements performed with a JPK Nanowizard 4 in a tapping mode with silicon tips over a scanned area of 60×60 µm². Raman spectra were measured with a Horiba LabRAM HR device equipped with an argon-ion laser operating at 514 nm wavelength. 2D XRD patterns were recorded using a Bruker D8 Discover diffractometer with an Eiger 2500k detector using CuKα radiation. The optical images of the top and bottom view of the free-

standing intrinsic diamond were taken by a digital microscope (VHX-6000, Keyence, Belgium) and the photo of the final heteroepitaxial SC-BDD electrodes was captured by an EOS M50 Canon camera.

2.3. Electrochemical measurements

Electrochemical measurements, including CV, differential pulse voltammetry (DPV) and Mott-Schottky analysis, were carried out using an Autolab PGSTAT 128N equipped with the FRA module and controlled by Nova 2.1 software (Metrohm, The Netherlands) in a home-built cylindrical PTFE cell (100 mL). A standard three-electrode set-up was used in which an Ag/AgCl (3 M KCl) and a 5.7 cm long platinum wire (both obtained from ALS Co, Japan) served as the reference and the counter electrode, respectively. The heteroepitaxially grown SC-BDD samples and poly-BDD electrode were employed as the working electrode. A free-standing poly-BDD sample (1.5×1.5 cm², 0.7 mm thickness, and [B] of 3×10^{20} cm^{-3} [33]) originating from Diafilm EP Grade BDD (Element Six, UK) was obtained from Mintres B.V. (The Netherlands). The growth side of the poly-BDD subjected to examination was chemically mechanically polished until a surface roughness of ~5 nm was reached.

The BDD-based working electrode was placed in the PTFE cell from underneath and sealed by a chemically resistant O-ring (Kalrez® Spectrum™ 6375, model AS568), while a geometrical area of 0.22 cm² was exposed to the measuring solution. The current densities reported in this work were calculated using the O-ring defined geometric area. Since the heteroepitaxial SC-BDD electrodes are only one-side doped, electric contact to the doped-surface was realized with conductive silver paint, applied from the four corners towards the backside, and contacted by a copper disc wired to the potentiostat.

To ensure satisfactory surface cleanliness and repeatability of the measurements, all BDD electrodes were cleaned and pre-treated in the same way. In the first step, BDD electrodes were boiled for 5 min in an acid mixture prepared by mixing concentrated HCl, H_2SO_4, and HNO_3 in a ratio of 2:2:3, which generated a highly stable O-terminated surface [34]. Previous studies showed that hydroxyl/ether (-C-O-H/-C-O-C) and carbonyl (>C=O) groups are the most abundant oxygen functionalities

present on the oxidized (100)-oriented crystal facet [23,35]. The second step involved ultra-sonication of the oxidized BDD samples in acetone, isopropanol, and deionized water, in each medium for 5 min. Lastly, the electrodes were subjected to 20 consecutive CV scans in the potential range from 0 V to +1.0 V in 0.1 M KNO_3 at a scan rate of 0.1 V s^{-1} to stabilize the baseline. Also, at the beginning of every measuring day, the BDD samples were anodically treated and renewed by applying a high positive potential of +2.5 V for 15 min in 0.1 M H_2SO_4.

Further, CVs were recorded in 0.1 M KNO_3 in the potential range between 0 V and +1.0 V and the following equation (Eq. (1)) was employed to estimate C_{dl} values:

$$C_{dl} = \Delta I_{AV} / A_{geom} \, v \qquad (Eq. \ 1)$$

where ΔI_{AV} (in A) is the average background current difference between the forward and reversed scan at a potential of +0.5 V, A_{geom} represents the geometric surface area (0.22 cm^2), and v is the scan rate (0.1 V s^{-1}).

To probe the anti-fouling property of the electrodes, CV experiments were performed in a solution of 1 mM AQDS in 0.1 M $HClO_4$ ($n = 20$, at a scan rate of 0.1 V s^{-1}). Next, electrodes were rinsed 5 times with deionized water to remove weakly adsorbed species. After rinsing, the electrodes were immersed only in 0.1 M $HClO_4$ (without AQDS) to repeat the CV measurements. This set of experiments was performed not only with BDD-based electrodes but also with a glassy carbon electrode (GCE, A_{geom} of 0.20 cm^2; obtained from ALS Co, Japan) pre-treated by polishing on alumina slurry.

DP voltammograms were recorded using a pulse amplitude of +50 mV, pulse width of 80 ms, potential step of 10 mV and a scan rate of 20 mV s^{-1}. The concentration dependences were plotted from the average of four replicate DPV measurements for each dopamine standard solution and evaluated by the least squares linear regression method. Limits of detection (LOD) were calculated as a threefold and limits of quantification (LOQ) as a tenfold of the standard deviation of the intercept, divided by the slope of corresponding calibration plot.

The Mott-Schottky (MS) plots were measured in 0.1 M KNO_3 solution in the potential range from −0.4 V to +0.8 V at a frequency of 160 Hz, and subsequently the Mott-Schottky equation (Eq. (2)) was used to estimate charge carrier concentration (N_A) [36]:

$$N_A = -2 \, / \, (e\varepsilon_0\varepsilon_r A^2[d(C_p^{-2})/dE]) \qquad (Eq. \ 2)$$

where e is an elementary charge, ε_0 is the permittivity of vacuum, ε_r is the relative permittivity of diamond material, A is the electrode area, and C_p^{-2} is the capacitance obtained at various potential values E. C_p values were evaluated from impedance data (1 Hz–25 kHz frequency range, 10 mV amplitude) fitted with simplified Randles equivalent circuit depicted in Fig. S1.

SECM measurements were conducted using a Scanning Electrochemical Workstation Model 370 (Ametek Scientific Instruments, USA) to evaluate the (in)homogeneous distribution of electrochemical activity of the different BDD surfaces. A four-electrode cell was used with a Pt microelectrode probe tip (10 μm diameter) and the BDD samples as working electrodes (WE1 - Pt and WE2 - BDD). The cell was completed with an Ag/AgCl (3 M KCl) and a Pt wire serving as the reference and the counter electrode, respectively. The SECM was operated under feedback mode using 1 mM $[Ru(NH_3)_6]^{3+/2+}$ (0.1 M KNO_3) as a redox mediator. The redox potential used for the reduction of the mediator at the Pt microprobe tip was −0.4 V. At the same time, the BDD samples were polarized at 0 V.

Approach curves were carried out to elucidate the electrochemical nature of the BDD surface (active or inactive). The Pt probe tip was carefully approached to the substrate (BDD surface) in the feedback mode at a rate of 0.1 μm s^{-1}. Whether the reduced species diffuse to an electrochemically active (conductive) or inactive (non-conductive) site on the BDD electrodes, the Pt probe shows a positive or negative feedback response, respectively. The positive feedback results from the oxidation of the mediator at the conductive sites. Curves were displayed

using normalised current (I) and distance (L). I corresponds to the ratio between the measured probe current (i_T) and the steady-state current ($i_{T\infty}$) recorded far from the substrate. L represents the ratio between substrate-to-probe tip distance (d) and the tip radius (r). The SECM maps of the BDD electrodes were recorded in an area of 60 × 60 μm^2 with a scanning rate of 5 μm s^{-1}, while the tip-substrate distance was fixed to 20 μm.

The electroanalytical measurements were carried out at room temperature (23 ± 1 °C). All reported potential values are referred to the Ag/AgCl electrode.

2.4. Chemicals

Hexaammineruthenium(III) chloride (≥98.0%), potassium hexacyanoferrate(II) trihydrate (≥98.5%), potassium nitrite (≥99.0%), sulphuric acid (95.0–98.0%), hydrochloric acid (37%), nitric acid (70%), phosphate buffered saline (powder, pH 7.4), isopropanol, acetone, disodium anthraquinone-2,6-disulfonate (AQDS, ≥97.0%), and dopamine hydrochloride (≥98.0%) were purchased from Merck and used without any further purification. Deionized water, ultra-filtrated with a Millipore Milli-Q system (resulting resistivity of 18.2 MΩ cm), was used to prepare all aqueous solutions.

3. Results and discussion

3.1. Surface characterization

The surface morphology of all SC-BDD and poly-BDD electrodes was observed by SEM and AFM; the representative micrographs are depicted in Fig. 2. Moreover, AFM provided information on the arithmetic mean surface roughness (S_a) and the values are summarized in Table 1.

Variations in surface morphological features of the individual heteroepitaxial SC-BDD electrodes can be clearly distinguished in Fig. 2. Samples A and B possess similar absolute values in surface roughness; however, the characteristic features are completely different. On the SC-BDD A, the surface is dominated by polishing lines owing to the rough mechanical polishing of the top side of the heteroepitaxial diamond quasi-substrate. Between the polishing lines the surface is very flat indicating that growth is controlled by lateral step flow. On the other hand, the features identified on the SC-BDD B sample grown on the back surface close to the diamond nucleation layers apparently reflect the small angle grain boundary structure typical for heteroepitaxial diamond after several micron growth. The on-axis SC-BDD C sample shows round hillocks. They are typical for 3D on-axis growth when the absence of an off-axis angle prevents an efficient step-flow growth mode. With a height of ~10 nm and lateral dimension of ~1 μm, these hillocks are still quite flat (see Fig. 2(iii)). As expected, relatively large crystal facets with clearly visible grain boundaries can be observed on the poly-BDD surface, which demonstrates its heterogeneous nature resulting from the growth process. Nevertheless, the surface roughness of poly-BDD is comparable to the values obtained for SC-BDD samples due to the applied chemical-mechanical polishing.
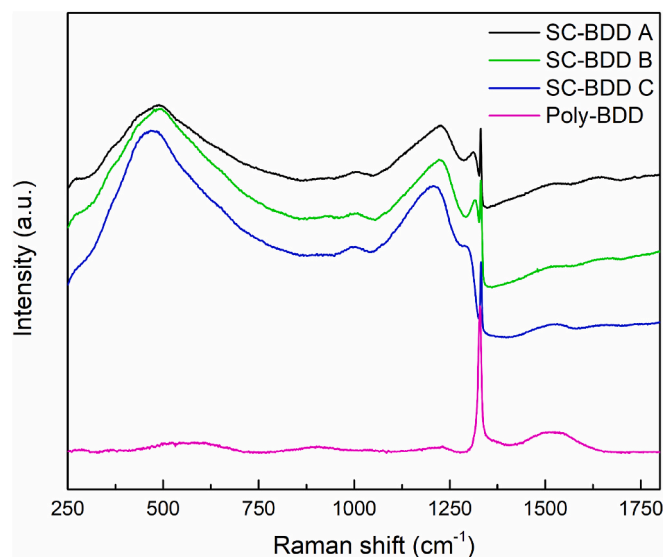
Next, Raman spectroscopy was employed to assess the composition and quality of the BDD electrodes and to evaluate their boron content. The common feature of the recorded Raman spectra for all samples (displayed in Fig. 3) is the sharp diamond peak located at 1332 cm^{-1}. In addition, the Raman spectra recorded from the heteroepitaxial SC-BDD electrodes exhibit two strong features reflecting boron incorporation into the diamond lattice and indicating heavily doped diamond: (i) the intense broad band at around 480 cm^{-1} attributable to a combination of electronic Raman scattering and a Fano-shaped band [37], and (ii) the asymmetric band centred at *ca* 1200 cm^{-1} originating from the phonon density of states [38]. Both characteristic peaks, however, much less pronounced, can be identified in the spectrum of poly-BDD, which also includes the G-band at 1580 cm^{-1} resulting from graphitic sp^2 carbon still present in the grain boundaries [39,40], despite the acid and anodic
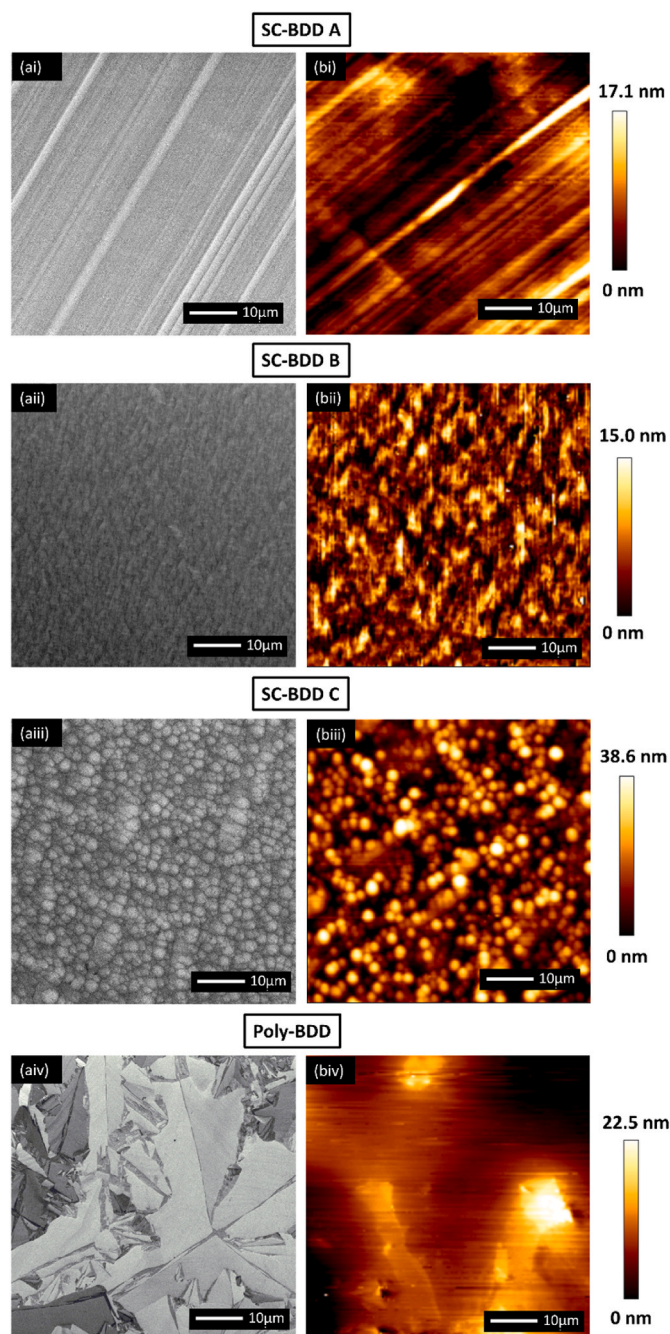
Fig. 2. (a) SEM images and (b) AFM images visualizing surface morphology of (i) SC-BDD A, (ii) SC-BDD B, (iii) SC-BDD C, and (iv) poly-BDD electrodes. (A colour version of this figure can be viewed online.)

Fig. 3. Raman spectra of (—) SC-BDD A, (—) SC-BDD B, (—) SC-BDD C, and (—) poly-BDD.

oxidation treatments [41]. In contrast, the absence of the G-band peak in the Raman spectra of the heteroepitaxial SC-BDD samples indicates that the monocrystalline electrodes are largely free of sp^2 carbon impurities, and are thus of a very high phase purity.

Moreover, the fitting tool [42], based on the analysis of the two Raman peaks located at ~1200 cm^{-1} and ~1332 cm^{-1}, was used for [B] determination. The assessed [B], overviewed in Table 1, range between $(2.5–4.4) \times 10^{21}$ cm^{-3} for the heteroepitaxial SC-BDD samples and prove their heavy boron doping level and metal-like character. For the poly-BDD electrode, [B] was calculated to be 1.8×10^{20} cm^{-3}, which correlates well with the value declared by the manufacturer (3×10^{20} cm^{-3} [33]).

The crystal plane orientations of the heteroepitaxially grown SC-BDD electrodes were studied using 2D XRD patterns, presented in Fig. 4. All SC-BDD samples show Bragg diffraction peaks corresponding to (400) diamond around 2θ = 120° (peak separation due to CuKα1 and CuKα2), confirming their single crystal nature and (100) orientation. However, as Fig. 4(b) shows, only the spot from SC-BDD C is almost in the middle along χ indicating its on-axis (100) orientation. On the other hand, the spots from SC-BDD A and SC-BDD B are shifted from the centre, which is ascribed to the fact that samples A and B were grown on 4° off-axis (100)-oriented quasi-substrates, and thus their surfaces are not exactly perpendicular to the (100) plane (see Fig. S2 schematically showing the 2D XRD measurement geometry). The 2D image of poly-BDD shows rings, indicating individual crystals with various orientations, and thus confirming its polycrystalline character.

Table 1
Morphological and electrochemical characteristics of studied BDD electrodes.

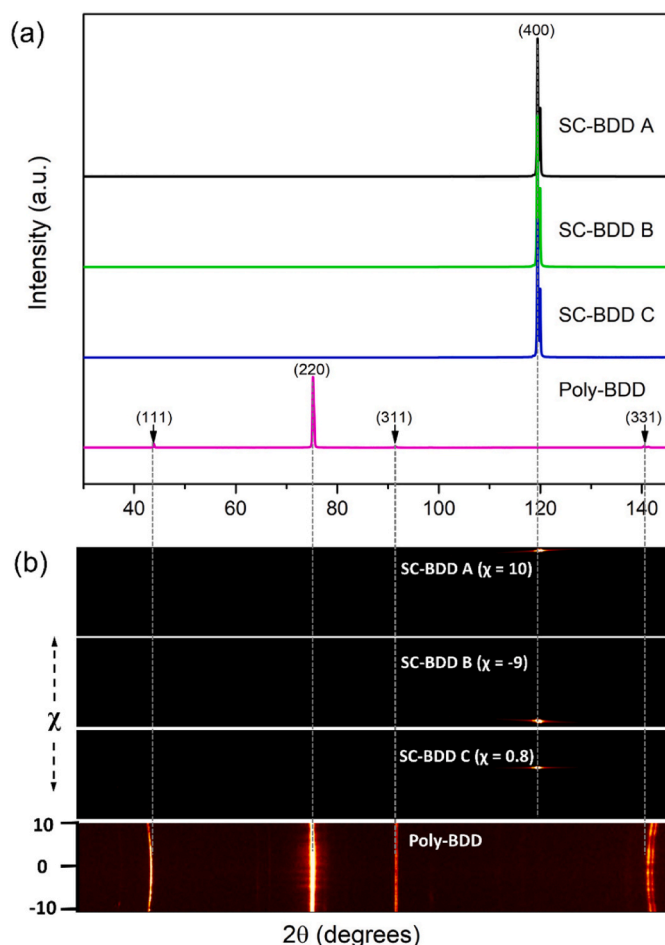| BDD electrode	SC-BDD A	SC-BDD B	SC-BDD C	Poly-BDD
Overall thickness (mm)	1.37	1.29	0.26	0.72
S_a (nm)	3.9	3.4	8.8	5.2
Potential window (V)	3.31	3.30	3.34	2.51
C_{dl} (μF cm^{-2})	3.5	3.7	3.9	4.6
[B]$_{Raman}$ (atoms cm^{-3})	2.7×10^{21}	2.5×10^{21}	4.4×10^{21}	1.8×10^{20}
[B]$_{MS}$ (atoms cm^{-3})	2.0×10^{21}	2.2×10^{21}	2.7×10^{21}	2.0×10^{20}
ΔE_p – [Ru(NH$_3$)$_6$]$^{3+/2+}$ (V)	0.067	0.068	0.067	0.067
ΔE_p – [Fe(CN)$_6$]$^{3-/4-}$ (V)	0.232	0.276	0.305	0.371
$E_{pA, DA}$ (V)	+0.637	+0.691	+0.752	+0.630
ΔE_p – DA/o-DQ (V)	0.642	0.703	0.793	0.673
Decrease in $I_{pA, DA}$ (for $n = 5$, %)	13.7	13.4	12.7	42.1

Fig. 4. (a) XRD patterns of (—) SC-BDD A, (—) SC-BDD B, (—) SC-BDD C, and (—) poly-BDD electrodes. (b) 2D XRD images captured on all BDD samples.

3.2. Electrochemical characterization in a supporting electrolyte

The width of the electrochemical potential window is a key property which determines the electrode's suitability and applicability for electrochemical sensing of a particular compound. Besides, both potential window and C_{dl} value provide valuable information about the surface condition of BDD electrodes, e.g., H- vs. O- termination [43] and sp^2 carbon presence [17]. For this reason, CV was performed in 0.1 M KNO$_3$ solution in the potential range from −1.5 to +2.5 V at a scan rate of 0.1 V s^{-1}, as shown in Fig. 5(a). Since nitrate (NO$_3^-$) reduction can only be achieved with a H-terminated BDD electrode [44] and all electrodes employed in this study were O-terminated, no interfering effects caused by the selected supporting electrolyte were recognized. The potential windows were assessed (reported in Table 1) between anodic and cathodic limiting potentials at which the current density exceeds a value of ±0.4 mA cm^{-2} indicating the onset of water decomposition [16,17] leading to formation of oxygen and hydrogen gases in the anodic and cathodic region, respectively. In general, BDD-based materials in aqueous electrolyte solutions exhibit high overpotentials for oxygen and hydrogen evolution reactions, whose mechanisms are thoroughly described in Refs. [45,46], which subsequently reflect in wide available potential ranges. This excellent property was also confirmed for all heteroepitaxial SC-BDD electrodes, which provided broad potential windows of ∼3.3 V (see Table 1). Presumably, O-termination of the electrode surfaces contributed to this high value, as the expansion of solvent windows has been observed on O-terminated BDD electrodes [17,34,43], compared to H-terminated ones. As shown in Fig. 5(a), the width of the potential window of the poly-BDD electrode is reduced to 2.5 V, while the narrowing practically occurs only in the anodic region where oxygen develops. This behaviour is attributed to the heterogeneous character of the poly-BDD surface also containing sp^2 carbon impurities, whose presence was confirmed by Raman spectroscopy (see Fig. 3). Sp^2 sites possess increased catalytic activity facilitating the water electrolysis, thus causing the shift of the oxygen evolution reaction towards lower potential values [47].

Subsequently, CVs were recorded in the same medium (0.1 M KNO$_3$, at a scan rate of 0.1 V s^{-1}) but within shorter potential range from 0 V to

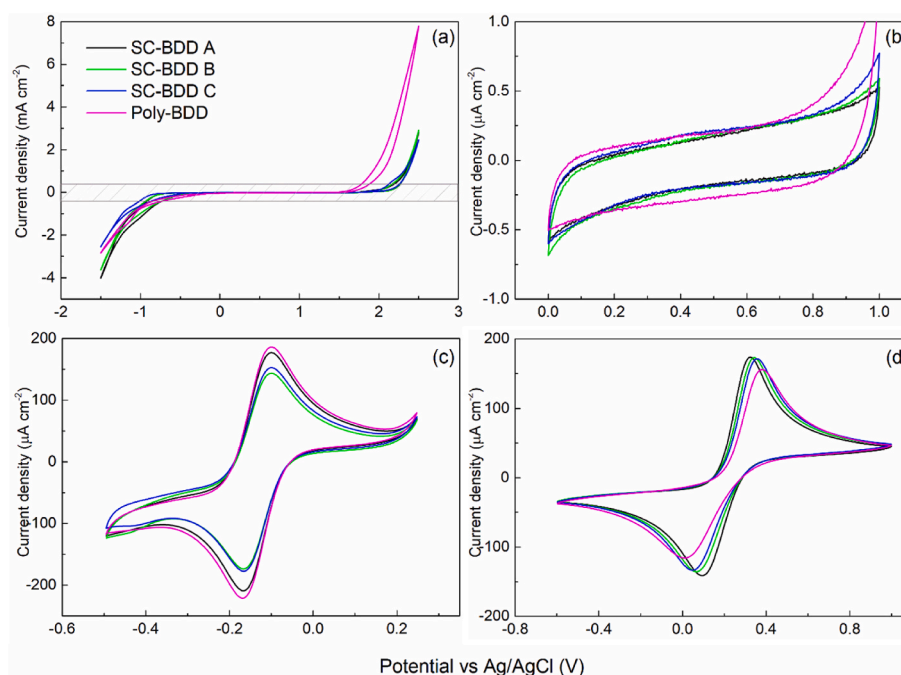**Fig. 5.** CVs recorded at a scan rate of 0.1 V s^{-1} on (—) SC-BDD A, (—) SC-BDD B, (—) SC-BDD C, and (—) poly-BDD in the following solutions: (a, b) 0.1 M KNO$_3$ in a range (a) from −1.5 V to +2.5 V, and (b) from 0 V to +1.0 V; (c) 1 mM [Ru(NH$_3$)$_6$]$^{3+/2+}$ in 0.1 M KNO$_3$, and (d) 1 mM [Fe(CN)$_6$]$^{3-/4-}$ in 0.1 M KNO$_3$. (A colour version of this figure can be viewed online.)

+1.0 V where only background (non-faradaic) currents flow, as depicted in Fig. 5(b). Based on these measurements, C_{dl} values were estimated using Eq. (1) and are reported in Table 1. All studied electrodes provided low and comparable C_{dl} values (<5 μF cm^{-2}), which is in a good agreement with C_{dl} values obtained on O-terminated BDD electrodes in neutral media in previous studies [16,46]. Besides, the C_{dl} of the BDD material indicates its quality. A high-quality BDD electrode typically provides a capacitance <10 μF cm^{-2} [17]. From observing Fig. 5(b) (and derived C_{dl} values), the newly fabricated heteroepitaxial SC-BDD electrodes can be considered of superior quality as compared to the high-quality poly-BDD. Also, lower C_{dl} values typically allow BDD electrodes to achieve lower detection limits toward selected analytes of interest. Therefore, combination of broad potential windows and low C_{dl} values implies promising potential and suitability of heteroepitaxial SC-BDD electrodes for electrochemical sensing.

To obtain information on the boron content present in the hetero-epitaxially grown SC-BDD electrodes, the MS plots were recorded according to the procedure described in Section 2.3. The linear part of the MS plots, displayed in Fig. S1, was identified and its slope was used in the Mott-Schottky equation (Eq. (2)) to determine boron carrier concentration [B], which is tabulated for every electrode in Table 1. It should be noted that the Helmholtz capacitance is neglected in the applied Randles equivalent circuit because its correction does not affect the slope of the MS plot (and thus subsequent [B] estimation), and only causes a displacement of the flat band potential [24].

The MS analysis yielded similar [B] values of $\sim 2 \times 10^{21}$ cm^{-3} for all three SC-BDD samples confirming their heavy boron doping and high conductivity. For poly-BDD, one order of magnitude lower [B] of 2×10^{20} cm^{-3} was estimated; this value corresponds well with [B] of 3×10^{20} cm^{-3} declared by the manufacturer [33]. Importantly, [B] values assessed using MS analysis are highly comparable with those extracted from the recorded Raman spectra (see Table 1). In addition, several previous works confirmed that the MS analysis can be favourably used for heavily boron-doped diamond electrodes [24,48] and gives reliable [B] values, which are similar to values obtained by Raman spectroscopy and neutron depth profiling [48].

3.3. Electrochemical characterization with redox markers

3.3.1. CV measurements

Electrochemical performance of the SC-BDD electrodes was further assessed, and compared to poly-BDD, using CV and two redox markers, $[Ru(NH_3)_6]^{3+/2+}$ and $[Fe(CN)_6]^{3-/4-}$ (both 1 mM in 0.1 M KNO$_3$); the recorded curves after iR compensation are presented in Fig. 5(c) and (d), respectively. All studied electrodes provided well-defined pairs of redox peaks for both markers. The most valuable parameter, *i.e.*, the peak-to-peak separation (ΔE_p), serves as ET rate indicator and was determined from the measurements; the values are provided in Table 1.

In general, $[Ru(NH_3)_6]^{3+/2+}$ is a representative of outer-sphere redox markers, which means that its redox reaction is controlled by simple diffusion and ET is not influenced by the electrode's surface characteristics such as surface termination, presence of sp^2 phase, and microstructure [49–52]. Importantly, $[Ru(NH_3)_6]^{3+/2+}$ due to its high sensitivity to the density of states [52] can be used as a probe to differentiate between 'metal-like' conductive (highly doped) and semi-conductive (lowly doped) BDD electrodes, as at the latter the ET kinetics of $[Ru(NH_3)_6]^{3+/2+}$ is significantly hindered [17]. On all SC-BDD electrodes, ΔE_p values for $[Ru(NH_3)_6]^{3+/2+}$ are similar and very close to 0.059 V (see Table 1), the value for a single electron reversible system. This confirms a near-reversible behaviour and fast ET kinetics of this redox couple, and consequently high quality and high conductivity of the SC-BDD electrodes, which is in a good agreement with the Mott-Schottky analysis indicating heavy boron doping (see Section 3.2). As expected, variations in surface morphology between the individual SC-BDD samples (described in Section 3.1) and O-termination do not affect redox behaviour of $[Ru(NH_3)_6]^{3+/2+}$ due to its outer-sphere nature.

In contrast, the second utilised redox probe, $[Fe(CN)_6]^{3-/4-}$, exhibits inner-sphere character and its redox reaction, occurring through specific surface interactions, is strongly dependent of BDD surface properties, predominantly surface termination, and boron doping level [46,50–52]. In contrast, ET kinetics of $[Fe(CN)_6]^{3-/4-}$ is not significantly affected by sp^2-bonded carbon impurities [52,53]. An increase in ΔE_p values (shown in Table 1) was observed on all SC-BDD and poly-BDD electrodes indicating slower ET kinetics of $[Fe(CN)_6]^{3-/4-}$ redox couple, compared to the outer-sphere probe, while the inhibition of ET can be ascribed to O-termination of the SC-BDD and poly-BDD electrodes [50,51]. Our results correlate well with prior studies reporting that ET kinetics of $[Fe(CN)_6]^{3-/4-}$ is hindered even on highly doped but O-terminated BDD surfaces [16,23]. This is caused by the presence of oxygen-containing groups being able to block adsorption sites [49] and/or electrostatically repel anionic redox probe, as oxygen groups possess negative charge $(C^{\delta+}-O^{\delta-})$ [50]. Furthermore, among all electrodes tested, the highest ΔE_p and thus the slowest kinetics along with a decrease in peak current density of $[Fe(CN)_6]^{3-/4-}$ (as shown in Fig. 5(d)) was observed on poly-BDD. Conversely, the fastest ET kinetics was recognized on the SC-BDD A electrode. Concerning only the SC-BDD electrodes, the rougher, on-axis sample C provided a higher ΔE_p value, compared to the smoother, 4° off-axis electrodes A and B.

In previous studies employing O-terminated (100), (110), and (111)-faceted monocrystalline diamond electrodes [14,23], much larger ΔE_p values ranging between 0.24 V–1.83 V for $[Ru(NH_3)_6]^{3+/2+}$ and 0.45 V–2.7 V for $[Fe(CN)_6]^{3-/4-}$ were obtained (see Table S1), which reflect very, in some cases even extremely, sluggish ET kinetics. In comparison with the mentioned works [14,23], herein reported heteroepitaxially grown SC-BDD electrodes with (100) orientation and O-termination demonstrated the best electrochemical performance. Such difference in electrochemical behaviour presumably arises from different dopant concentration and conductivity: the heteroepitaxially grown SC-BDD electrodes presented in this study possess high doping with [B] $\sim 2 \times 10^{21}$ cm^{-3} and thus high conductivity, while single crystal diamond electrodes used in Refs. [14,23] were less doped by almost one order of magnitude (as can be seen in Table S1), which caused lower conductivity manifested by slower ET kinetics.

Next, CVs of both redox markers were recorded on all electrodes in a range of scan rates from 0.025 V s^{-1} to 0.8 V s^{-1}; voltammograms are depicted in Fig. S3 for $[Ru(NH_3)_6]^{3+/2+}$ and Fig. S4 for $[Fe(CN)_6]^{3-/4-}$. The scan rate study revealed that the redox reactions of both redox markers are diffusion-controlled on all SC-BDD and poly-BDD electrodes as peak currents increased linearly with the square root of the scan rate (see Fig. S3(e) and Fig. S4(e)).

Finally, it needs to be emphasized that all heteroepitaxial SC-BDD electrodes provided comparable and highly satisfactory electrochemical performance, confirming their high quality as well as high conductivity. Apparently, the distinct variations in surface morphology, presented and discussed in Section 3.1, have only a minor effect on the behaviour of SC-BDD electrodes.

3.3.2. SECM measurements

The electrochemical homogeneities of the heteroepitaxial SC-BDD and poly-BDD electrode surfaces were studied by SECM operating in a feedback mode (Fig. 6). SECM maps of the samples were recorded by polarising the Pt probe tip at -0.4 V, which corresponds to the reduction potential of the selected mediator $[Ru(NH_3)_6]^{3+/2+}$ (see Fig. S5). At the same time, the sample, *i.e.*, a BDD electrode, was polarised at 0 V, which is the oxidation potential of the mediator in the case that the surface is active (conductive). The maps of the three heteroepitaxial SC-BDD samples showed similar behaviour. The current values measured at the probe are higher than the limiting current (in bulk solution), indicating that the surface electrodes are electrochemically active (conductive). In this case, with the proximity of the probe to the surface, the reduced mediator (Ru(III) → Ru(II)) at the tip can be oxidized back
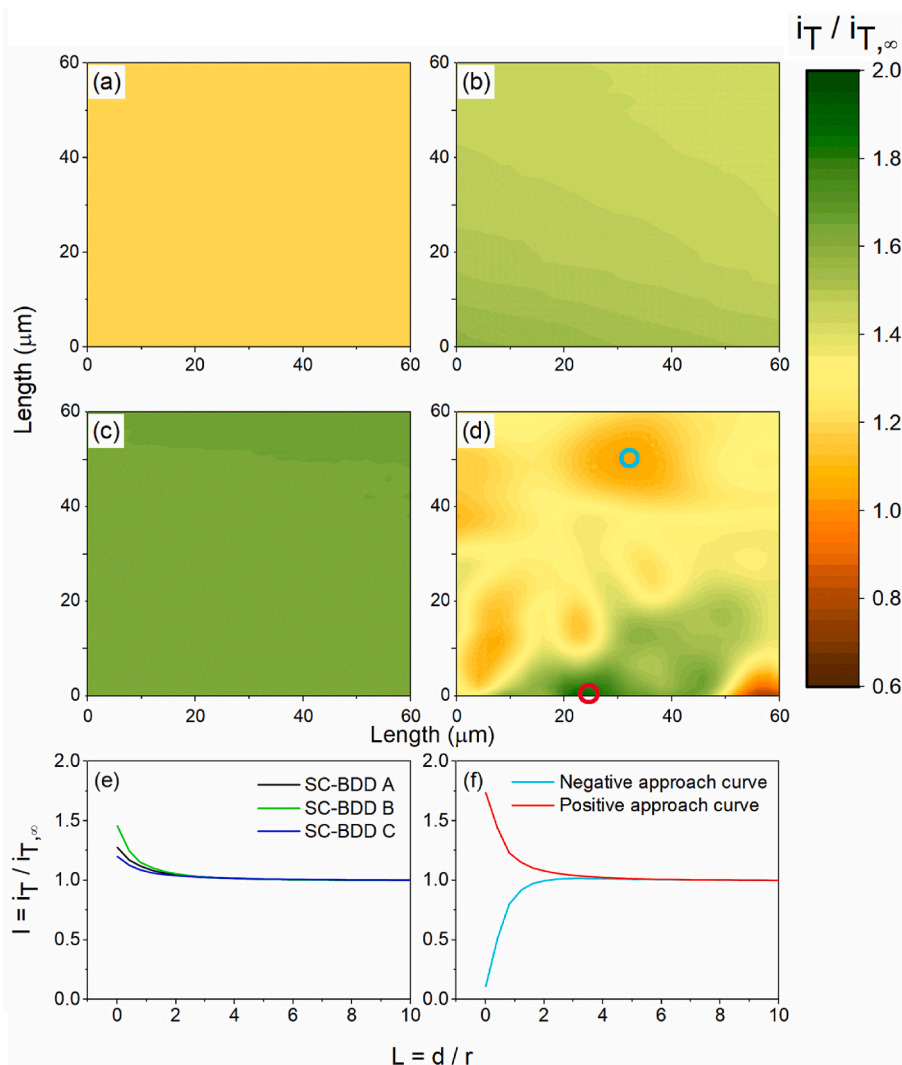
Fig. 6. SECM images of (a) SC-BDD A, (b) SC-BDD B, (c) SC-BDD C and (d) poly-BDD electrodes. All maps are scaled to a current window of 2.5 nA. The approach curves of (e) heteroepitaxial SC-BDD electrodes and (f) poly-BDD recorded at two different spots indicated by the cyan and red circles in (d). (A colour version of this figure can be viewed online.)

to Ru(III) at the substrate. The approach curve measurements also confirm the conductive nature of the SC-BDD surfaces. The curves were obtained by locating the probe at different random surface spots. The resulting curves showed a positive feedback response, in which the current increased when the probe approached the surface due to the regeneration of the redox mediator (Ru(III)). These can be seen in the selected approach curves shown in Fig. 6(e). In the case of the sample SC-BDD B, the map (Fig. 6(b)) showed a slight variation in current from top right to bottom left. This can be related to the tilt of the sample when placed in the electrochemical cell. This tilt causes a small change in the tip-substrate distance across the scanned area, resulting in a current variation. Nevertheless, the sample B clearly shows an electrochemically active response.

On the other hand, the poly-BBD electrode presented a different behaviour. The SECM map (Fig. 6(d)) showed a heterogeneous distribution of currents, with locations showing electrochemically active and non-active behaviour. The latter is associated with current values lower than the limiting current. In this case, the signal is influenced by the proximity of the substrate and the limited availability of the redox mediator. These heterogeneities cannot be associated with the topology of the surface. From the AFM analysis, it was estimated that the roughness of the surface is in the nanometer range (see Table 1). For the

SECM, the resolution is at the micrometer range, with a tip-substrate distance of ~20 μm. Hence, nanometric topological variations of the surface are out of the detection range of the probe.

Interestingly, localised current variations observed in the SECM map match with the distinctive dimension and distribution of the diamond grains shown in Fig. 2(iv). The grains present different electrochemical nature (active and non-active). This heterogeneity is likely attributed to the different boron incorporation efficiency of various crystal orientations [13,15,54]. To further confirm the heterogeneous nature of those locations, approach curves were measured at two selected spots as indicated in the SECM map of Fig. 6(d) (cyan and red circles). Positive and negative feedback responses can be clearly observed in the curves displayed in Fig. 6(f), confirming the active and non-active natures of those locations, respectively.

3.4. Voltammetric behaviour of dopamine on heteroepitaxial SC-BDD electrodes

To verify the applicability of fabricated SC-BDD electrodes for electrochemical sensing, CV experiments were performed with a commonly detected compound, dopamine (1 mM; in a 1 M phosphate buffered saline (PBS) of pH 7.4) of well-described redox behaviour [55].
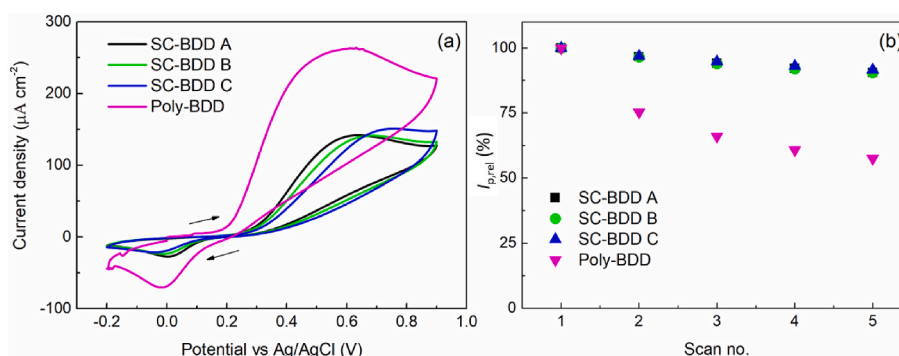
Fig. 7. (a) CVs recorded in a solution of 1 mM dopamine in a pH 7.4 PBS (1 M) at a scan rate of 0.1 V s^{-1} on (—) SC-BDD A, (—) SC-BDD B, (—) SC-BDD C, and (—) poly-BDD electrodes. (b) Relative peak heights of 1 mM dopamine in a pH 7.4 PBS (1 M) assessed from five consecutive CV scans recorded on SC-BDD and poly-BDD electrodes.

Measured voltammetric curves, including the one recorded on poly-BDD for comparison, are displayed in Fig. 7 and the parameters gained from the experiments are provided in Table 1.

CV curves recorded on all the electrodes display a quasi-reversible redox system as two peaks can be identified in the selected potential range from −0.2 V to +0.9 V. The anodic peak ($E_{pA, DA}$) appearing at a potential higher than +0.6 V corresponds to the dopamine oxidation to dopamine-*o*-quinone, while the cathodic peak developed at ∼0 V arises from the reduction of dopamine-*o*-quinone back to dopamine; both reactions involve the exchange of two electrons and two protons in a selected pH 7.4 buffer [55]. Overall, comparable electrochemical responses of dopamine were recorded on the SC-BDD electrodes; however, slight variations can be identified (see Table 1). The highest $E_{pA, DA}$ was registered on "on-axis" sample C with a rougher surface consisting of hillock-like features, which appear to have a hindering effect on dopamine oxidation reaction. In contrast, smaller $E_{pA, DA}$ was recorded on the smoother "off-axis" samples A and B.

Dopamine, due to its inner-sphere ET [52,56], is sensitive to the chemical composition of BDD electrode surfaces, *i.e.*, termination (H- *vs.* O-) [43,56–58] and sp^3/sp^2 ratio [56,59,60]. Herein obtained $E_{pA, DA}$ and large ΔE_p (Table 1) agree well with the values reported for dopamine on O-terminated BDD surfaces in previous studies carried out in the PBS media of pH 7.0–7.4 (see Table S2) [57,61,62]. Generally, dopamine oxidation is hindered on oxidized diamond electrodes, manifested by a shift in $E_{pA, DA}$ to more positive values in comparison with H-terminated BDD [43,57,58]. As further shown in Fig. 7(a), the SC-BDD electrodes provide anodic peaks of similar current densities, while on poly-BDD the dopamine peak height is almost twice that intense. Such an increase in the voltammetric signal of dopamine can be attributed to the heterogeneous nature of the poly-BDD surface also containing grain boundaries where sp^2 carbon typically resides (the presence of sp^2 impurities is derived from the Raman spectrum in Fig. 2). Sp^2 sites may act as spots for dopamine adsorption [20,56], facilitate its redox reaction and contribute to the increased currents.

Another significant difference between the SC-BDD and poly-BDD samples emerged when consecutive CV scans of dopamine were recorded, as is clearly visible in Fig. 7(b) and Fig. S6. A more pronounced decrease in both anodic and cathodic peak current densities occurred on poly-BDD; specifically, the oxidation peak current lowered by ∼42% within five consecutive scans due to the surface fouling by oxidation product(s), which blocks electroactive sites on the electrode [55,63]. In contrast, a much smaller decrease in peak heights of the dopamine/dopamine-*o*-quinone redox pair was recognized on the SC-BDD electrodes: the variation in anodic peak height ($I_{pA, DA}$) between the first and fifth scan was less than 14%. This clearly indicates enhanced resistance of heteroepitaxially grown SC-BDD samples towards electrode fouling.

Importantly, implementation of a simple stirring of the analysed
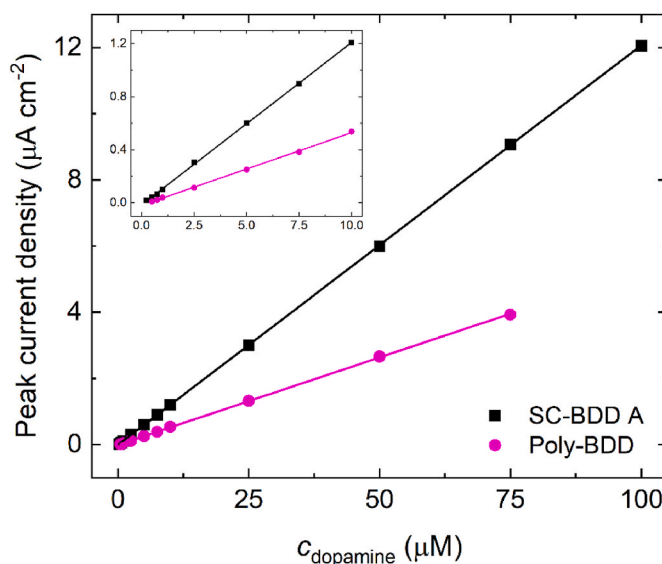
Fig. 8. Concentration dependences of dopamine recorded by DPV on oxidized SC-BDD A and poly-BDD electrodes. Inset shows detail of dependences for lower concentrations. (A colour version of this figure can be viewed online.)

dopamine solution (0.10 mM) between the individual CV scans ($n = 10$), acquired on freshly re-oxidized SC-BDD and poly-BDD electrodes, resulted in satisfactory repeatability, expressed by relative standard deviation (RSD) of the anodic peak heights of less than 2.6% for all four tested electrodes. Then, the same set of experiments was conducted two more times in 5-day intervals and RSD from all measurements ($n = 30$ in total) was evaluated to be 4.2% for SC-BDD A, 4.8% for SC-BDD B, 2.9% for SC-BDD C, and 4.0% for poly-BDD. Such RSD values reveal excellent stability of the recorded dopamine signals and indicate suitability of the SC-BDD electrodes for sensing applications.

Next, more sensitive voltammetric technique, DPV, was employed to record concentration dependences of dopamine in 10 mM PBS of pH 7.4 on the SC-BDD A, and for comparison purposes, also on the poly-BDD sample; the linear DP voltammetric responses for both electrodes are depicted in Fig. S7. Sample A was selected as a representative of heteroepitaxial SC-BDD because it manifested better electrochemical characteristics in the preceding measurements (see Table 1). Concentration dependences are plotted in Fig. 8 and the obtained analytical parameters along with calculated LOD and LOQ are summarized in Table 2. Clearly, the heteroepitaxial SC-BDD A electrode outperformed conventionally used poly-BDD because it demonstrated wider linear range, enhanced sensitivity and lower LOD and LOQ values. This

Table 2
Analytical parameters of dopamine concentration dependences recorded by DPV in 10 mM PBS (pH 7.4) on BDD-based electrodes, including calculated LOD and LOQ values.

Electrode	Linear range (μmol L^{-1})	Intercept $\times 10^{-2}$ (μA cm^{-2})	Slope $\times 10^{-2}$ (μA μM^{-1} cm^{-2})	R	LOD (μmol L^{-1})	LOQ (μmol L^{-1})
SC-BDD A	0.25–100.0	-1.66 ± 0.41	12.25 ± 0.01	0.9998	0.10	0.33
Poly-BDD	0.50–75.0	-1.93 ± 0.35	5.47 ± 0.07	0.9995	0.19	0.65

comparison further supports suitability and applicability of the newly developed heteroepitaxial SC-BDD electrodes for electroanalysis and sensor development.

3.5. Adsorption behaviour of AQDS

To further explore the anti-fouling property of heteroepitaxial SC-BDD electrodes, measurements were performed with AQDS, which can serve as an "adsorption marker". AQDS is well-known for its high adsorption ability, predominantly towards metallic and sp^2 carbon electrodes [64,65]; for the latter it was verified also in this study during experiments with AQDS on glassy carbon electrode (GCE; see Fig. S8 in Supplementary material).

In CVs of the SC-BDD electrodes (see Fig. 9(a)), only background currents were recorded in the potential range from -0.4 V to $+1.0$ V. Thus, no peaks were registered. On the poly-BDD, however, a couple of small and broad peaks can be recognized at potentials of $+0.15$ V and $+0.25$ V, which are ascribed to the quasi-reversible redox reaction of adsorbed AQDS [64]. Besides, a scan rate study was performed, during which the current densities of both peaks increased linearly with an increase in the scan rate, as can be seen in Fig. 9(b). This confirms that the AQDS reaction on poly-BDD is adsorption-controlled. CVs recorded on GCE, shown in Fig. S8, revealed much more intense symmetrical peaks with ΔE_p approaching 0 V, which correspond to the redox reaction of AQDS and reveal characteristic features of a surface-confined redox analyte. Similarly to the poly-BDD, the scan rate study proved that the AQDS reaction on GCE surface is controlled by adsorption. This correlates very well with the previously published works reporting the same observation for AQDS reaction on GCE [65].

In a previous study [65], the electrode surface chemistry was identified as the main factor responsible for AQDS adsorption. Polar surfaces containing oxygen functionalities are significantly more prone to adsorption through strong dipole-dipole and ion-dipole interactions, which can be formed between AQDS molecules and the oxidized surfaces. Nevertheless, all four electrodes used in this study and subjected to experiments with AQDS were oxidized, and thus polar oxygen-containing groups were introduced on their surfaces. Interestingly, the heteroepitaxial SC-BDD electrodes in their O-terminated state showed resistance towards AQDS adsorption despite their polar and hydrophilic character. This indicates that another factor, presumably

the complex heterogeneous nature of the poly-BDD surface with grain boundaries, sp^2 carbon and growth defects, weakens the diamond electrode ability to resist adsorption. Moreover, a similar observation was made in Ref. [22] where a (111)-oriented SC-BDD electrode showed a lower tendency for adsorption than mechanically polished poly-crystalline BDD; the absence of defects and sp^2 carbon impurities on the single-crystal diamond surface was identified as the main factor contributing to the resistance towards adsorption.

All in all, heteroepitaxial SC-BDD represents a very attractive electrode material with suitable electrochemical performance and excellent anti-fouling characteristics resulting in improved response stability. Consequently, SC-BDD certainly has the potential and ability to replace and even outperform conventional poly-BDD, particularly in applications where low susceptibility towards (bio)fouling is extremely important, *e.g.*, for *in-vitro* and *in-vivo* sensing [63].

4. Conclusion and outlook

In the present study, a highly promising concept of heteroepitaxial growth for the preparation of large-area, heavily doped (100)-faceted SC-BDD electrodes has been successfully demonstrated. Three fabricated SC-BDD samples were subjected to detailed surface analysis and electrochemical characterization, and their properties were compared to the conventional poly-BDD.

2D XRD images confirmed the single crystal nature and the orientation of SC-BDD samples, while SEM and AFM micrographs visualized variations in the surface morphology. Absence of sp^2 carbon impurities along with heavy doping ($[B] > 10^{21}$ cm^{-3}) of the heteroepitaxial SC-BDD electrodes was demonstrated by Raman spectroscopy and MS analysis, respectively. Highly conductive, 'metal-like' nature of the SC-BDD electrodes was further confirmed by CV experiments with $[Ru(NH_3)_6]^{3+/2+}$ probe manifesting near-reversible redox response and almost ideal ΔE_p (0.067 V) approaching 0.059 V. In addition to the fast ET kinetics, wide potential windows (~3.3 V) and low C_{dl} values (<4 μF cm^{-2}) confirmed superior quality, compared to poly-BDD, and excellent electrochemical characteristics of the newly developed SC-BDD electrodes. Only CV experiments with surface sensitive $[Fe(CN)_6]^{3-/4-}$ and dopamine/dopamine-*o*-quinone redox systems demonstrated minor impact of the morphological features, dislocation density and small off-cut angle on the electrochemical behaviour of SC-BDD. Nevertheless,
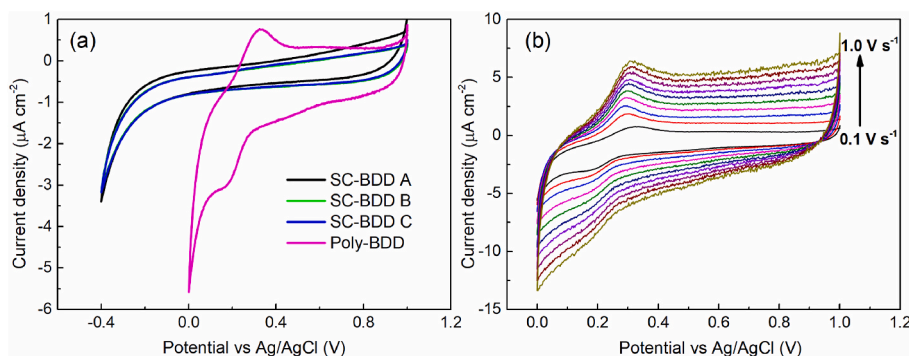
Fig. 9. CVs recorded in 0.1 M $HClO_4$ after experiments with 1 mM AQDS and subsequent thorough rinsing with deionized water: (a) on (—) SC-BDD A, (—) SC-BDD B, (—) SC-BDD C, and (—) poly-BDD electrodes at a scan rate of 0.1 V s^{-1}, and (b) on poly-BDD at different scan rates.. (A colour version of this figure can be viewed online.)

small variations could be still identified: Interestingly, the rougher, "on-axis" sample C provided higher ΔE_p values, indicating slower ET kinetics, for both tested inner-sphere markers, while smaller ΔE_p were recorded on the smoother 4° "off-axis" samples A and B. As a result, the heteroepitaxial SC-BDD A sample was further subjected to DPV recording of dopamine concentration dependence and exhibited more satisfactory analytical parameters (wider linear range, enhanced sensitivity and lower LOD and LOQ values) than conventional poly-BDD electrode. In addition, the anti-fouling property of all SC-BDD electrodes was clearly demonstrated during experiments with dopamine and AQDS probe.

As a result, the overall electrochemical performance of the hetero-epitaxial SC-BDD samples is relatively comparable and highly satisfactory. This electrode material seems to be very attractive for electrochemical sensing, particularly in applications requiring strong resistance towards fouling and adsorption effects, manifesting by stable and reliable electrochemical responses; among such applications belong, *e.g.*, continuous monitoring of biomarkers and pharmaceuticals, *in-vitro* and *in-vivo* sensing. Moreover, heteroepitaxial SC-BDD certainly demonstrated a potential to outperform and replace conventional poly-BDD, suffering from its inherent heterogeneous and defective nature with sp^2 carbon impurities residing in the grain boundaries and often being responsible for deteriorated electrochemical performance, which can manifest by, *e.g.*, increased susceptibility towards adsorption and fouling effects.

Finally, heteroepitaxy-based approach enables the synthesis of high surface area SC-BDD electrodes, which could lead to much broader use of SC-BDD not only in electroanalysis, but also in other electrochemical fields, *e.g.*, waste-water treatment *via* advanced oxidation processes, electrosynthesis and electrocatalysis, for which scaling up is crucial. All in all, the heteroepitaxial SC-BDD offers possibilities that neither homoepitaxial single-crystal nor polycrystalline BDD electrodes have, *i.e.*, scalability (including large area) combined with controlled and well-defined surface orientation.

CRediT authorship contribution statement

Zhichao Liu: Conceptualization, Investigation, Formal analysis, Visualization, Writing – original draft. **Simona Baluchová:** Formal analysis, Writing – original draft, Writing – review & editing. **André F. Sartori:** Conceptualization, Resources, Writing – review & editing. **Ziyu Li:** Investigation, Formal analysis. **Yaiza Gonzalez-Garcia:** Resources, Writing – review & editing. **Matthias Schreck:** Resources, Writing – review & editing. **Josephus G. Buijnsters:** Conceptualization, Supervision, Writing – review & editing, Funding acquisition, Project administration.

Declaration of competing interest

The authors declare that they have no known competing financial interests or personal relationships that could have appeared to influence the work reported in this paper.

Acknowledgements

Appendix A. Supplementary data

Supplementary data to this article can be found online at https://doi.org/10.1016/j.carbon.2022.10.023.

References

[1] N.J. Yang, S.Y. Yu, J.V. Macpherson, Y. Einaga, H.Y. Zhao, G.H. Zhao, G.M. Swain, X. Jiang, Conductive diamond: synthesis, properties, and electrochemical applications, Chem. Soc. Rev. 48 (2019) 157–204, https://doi.org/10.1039/c7cs00757d.

[2] S. Baluchova, A. Danhel, H. Dejmkova, V. Ostatna, M. Fojta, K. Schwarzova-Peckova, Recent progress in the applications of boron doped diamond electrodes in electroanalysis of organic compounds and biomolecules - a review, Anal. Chim. Acta 1077 (2019) 30–66, https://doi.org/10.1016/j.aca.2019.05.041.

[3] M. Yence, A. Cetinkaya, G. Ozcelikay, S.I. Kaya, S.A. Ozkan, Boron-doped diamond electrodes: recent developments and advances in view of electrochemical drug sensors, Crit. Rev. Anal. Chem. (2021) 17, https://doi.org/10.1080/10408347.2020.1863769.

[4] Y.P. He, H.B. Lin, Z.C. Guo, W.L. Zhang, H.D. Li, W.M. Huang, Recent developments and advances in boron-doped diamond electrodes for electrochemical oxidation of organic pollutants, Separ. Purif. Technol. 212 (2019) 802–821, https://doi.org/10.1016/j.seppur.2018.11.056.

[5] O.M. Cornejo, M.F. Murrieta, L.F. Castaneda, J.L. Nava, Characterization of the reaction environment in flow reactors fitted with BDD electrodes for use in electrochemical advanced oxidation processes: a critical review, Electrochim. Acta 331 (2020) 14, https://doi.org/10.1016/j.electacta.2019.135373.

[6] D.S. Babu, J.M.C. Mol, J.G. Buijnsters, Experimental insights into anodic oxidation of hexafluoropropylene oxide dimer acid (GenX) on boron-doped diamond anodes, Chemosphere 288 (2022) 10, https://doi.org/10.1016/j.chemosphere.2021.132417.

[7] R.C.P. Oliveira, J.G. Buijnsters, M.M. Mateus, J.C.M. Bordado, D.M.F. Santos, On the electrooxidation of kraft black liquor on boron-doped diamond, J. Electroanal. Chem. 909 (2022), 116151, https://doi.org/10.1016/j.jelechem.2022.116151.

[8] S. Lips, S.R. Waldvogel, Use of boron-doped diamond electrodes in electro-organic synthesis, Chemelectrochem 6 (2019) 1649–1660, https://doi.org/10.1002/celc.201801620.

[9] C.Y. Guo, J.G. Zheng, H.W. Deng, P.H. Shi, G.H. Zhao, Photoelectrocatalytic interface of boron-doped diamond: modification, functionalization and environmental applications, Carbon 175 (2021) 454–466, https://doi.org/10.1016/j.carbon.2020.12.027.

[10] S.Y. Yu, N.J. Yang, S.T. Liu, X. Jiang, Diamond supercapacitors: progress and perspectives, Curr. Opin. Solid State Mater. Sci. 25 (2021) 13, https://doi.org/10.1016/j.cossms.2021.100922.

[11] D.J. Garrett, W. Tong, D.A. Simpson, H. Meffin, Diamond for neural interfacing: a review, Carbon 102 (2016) 437–454, https://doi.org/10.1016/j.carbon.2016.02.059.

[12] P.A. Nistor, P.W. May, Diamond thin films: giving biomedical applications a new shine, J. R. Soc. Interface 14 (2017) 15, https://doi.org/10.1098/rsif.2017.0382.

[13] G. Janssen, W.J.P. van Enckevort, W. Vollenberg, L.J. Giling, Characterization of single-crystal diamond grown by chemical vapour deposition processes, Diam. Relat. Mater. 1 (1992) 789–800, https://doi.org/10.1016/0925-9635(92)90102-T.

[14] Y.V. Pleskov, Y.E. Evstefeeva, M.D. Krotova, V.P. Varnin, I.G. Teremetskaya, Synthetic semiconductor diamond electrodes: electrochemical behaviour of homoepitaxial boron-doped films orientated as (111), (110), and (100) faces, J. Electroanal. Chem. 595 (2006) 168–174, https://doi.org/10.1016/j.jelechem.2006.07.010.

[15] N.R. Wilson, S.L. Clewes, M.E. Newton, P.R. Unwin, J.V. Macpherson, Impact of grain-dependent boron uptake on the electrochemical and electrical properties of polycrystalline boron doped diamond electrodes, J. Phys. Chem. B 110 (2006) 5639–5646, https://doi.org/10.1021/jp0547616.

[16] L.A. Hutton, J.G. Iacobini, E. Bitziou, R.B. Channon, M.E. Newton, J.V. Macpherson, Examination of the factors affecting the electrochemical performance of oxygen-terminated polycrystalline boron-doped diamond electrodes, Anal. Chem. 85 (2013) 7230–7240, https://doi.org/10.1021/ac401042t.

[17] J.V. Macpherson, A practical guide to using boron doped diamond in electrochemical research, Phys. Chem. Chem. Phys. 17 (2015) 2935–2949, https://doi.org/10.1039/c4cp04022h.

[18] J. Ryl, A. Zielinski, R. Bogdanowicz, K. Darowicki, Heterogeneous distribution of surface electrochemical activity in polycrystalline highly boron-doped diamond electrodes under deep anodic polarization, Electrochem. Commun. 83 (2017) 41–45, https://doi.org/10.1016/j.elecom.2017.08.019.

[19] T. Watanabe, S. Yoshioka, T. Yamamoto, H. Sepehri-Amin, T. Ohkubo, S. Matsumura, Y. Einaga, The local structure in heavily boron-doped diamond and the effect this has on its electrochemical properties, Carbon 137 (2018) 333–342, https://doi.org/10.1016/j.carbon.2018.05.026.

[20] S. Garcia-Segura, E. Vieira dos Santos, C.A. Martínez-Huitle, Role of sp3/sp2 ratio on the electrocatalytic properties of boron-doped diamond electrodes: a mini review, Electrochem. Commun. 59 (2015) 52–55, https://doi.org/10.1016/j.elecom.2015.07.002.

[21] R. Ramesham, Cyclic voltammetric response of boron-doped homoepitaxially grown single crystal and polycrystalline CVD diamond, Sens. Actuator B-Chem. 50 (1998) 131–139, https://doi.org/10.1016/s0925-4005(98)00214-7.

[22] T. Kondo, Y. Einaga, B.V. Sarada, T.N. Rao, D.A. Tryk, A. Fujishima, Homoepitaxial single-crystal boron-doped diamond electrodes for electroanalysis, J. Electrochem. Soc. 149 (2002) E179–E184, https://doi.org/10.1149/1.1471548.

[23] T.A. Ivandini, T. Watanabe, T. Matsui, Y. Ootani, S. Iizuka, R. Toyoshima, H. Kodama, H. Kondoh, Y. Tateyama, Y. Einaga, Influence of surface orientation on electrochemical properties of boron-doped diamond, J. Phys. Chem. C 123 (2019) 5336–5344, https://doi.org/10.1021/acs.jpcc.8b10406.

[24] L. Kavan, Z. Vlckova Zivcova, V. Petrak, O. Frank, P. Janda, H. Tarabkova, M. Nesladek, V. Mortet, Boron-doped diamond electrodes: electrochemical, atomic force microscopy and Raman study towards corrosion-modifications at nanoscale, Electrochim. Acta 179 (2015) 626–636, https://doi.org/10.1016/j.electacta.2015.04.124.

[25] A. Taylor, S. Baluchová, L. Fekete, L. Klimša, J. Kopeček, D. Šimek, M. Vondráček, L. Míka, J. Fischer, K. Schwarzová-Pecková, V. Mortet, Growth and comparison of high-quality MW PECVD grown B doped diamond layers on {118}, {115} and {113} single crystal diamond substrates, Diam. Relat. Mater. 123 (2022) 108815, https://doi.org/10.1016/j.diamond.2021.108815.

[26] A. Tallaire, A. Valentin, V. Mille, L. William, M.A. Pinault-Thaury, F. Jomard, J. Barjon, J. Achard, Growth of thick and heavily boron-doped (113)-oriented CVD diamond films, Diam. Relat. Mater. 66 (2016) 61–66, https://doi.org/10.1016/j.diamond.2016.03.020.

[27] J.-C. Arnault, S. Saada, V. Ralchenko, Chemical vapor deposition single-crystal diamond: a review, Phys. Status Solidi RRL 16 (2022), 2100354, https://doi.org/10.1002/pssr.202100354.

[28] M. Schreck, S. Gsell, R. Brescia, M. Fischer, Ion bombardment induced buried lateral growth: the key mechanism for the synthesis of single crystal diamond wafers, Sci. Rep. 7 (2017), 44462, https://doi.org/10.1038/srep44462.

[29] A.F. Sartori, M. Fischer, S. Gsell, M. Schreck, In situ boron doping during heteroepitaxial growth of diamond on Ir/YSZ/Si, Phys. Status Solidi 209 (2012) 1643–1650, https://doi.org/10.1002/pssa.201200221.

[30] A.F. Sartori, Heteroepitaxial Boron-Doped Diamond: from Synthesis to Application, Universität Augsburg, Augburg, Germany, 2016, p. 235.

[31] M. Mayr, M. Fischer, O. Klein, S. Gsell, M. Schreck, Interaction between surface structures and threading dislocations during epitaxial diamond growth, Phys. Status Solidi 212 (2015) 2480–2486, https://doi.org/10.1002/pssa.201532243.

[32] C. Stehl, M. Fischer, S. Gsell, E. Berdermann, M.S. Rahman, M. Traeger, O. Klein, M. Schreck, Efficiency of dislocation density reduction during heteroepitaxial growth of diamond for detector applications, Appl. Phys. Lett. 103 (2013), 151905, https://doi.org/10.1063/1.4824330.

[33] Element Six, E.P. Diafilm™, A Solid Solution for Sanitising and Electrochemical Processing, 2020.

[34] F.B. Liu, J.D. Wang, B. Liu, X.M. Li, D.R. Chen, Effect of electronic structures on electrochemical behaviors of surface-terminated boron-doped diamond film electrodes, Diam. Relat. Mater. 16 (2007) 454–460, https://doi.org/10.1016/j.diamond.2006.08.016.

[35] S. Ghodbane, D. Ballutaud, F. Omnès, C. Agnès, Comparison of the XPS spectra from homoepitaxial {111}, {100} and polycrystalline boron-doped diamond films, Diam. Relat. Mater. 19 (2010) 630–636, https://doi.org/10.1016/j.diamond.2010.01.014.

[36] A.F. Azevedo, M.R. Baldan, N.G. Ferreira, Doping level influence on chemical surface of diamond electrodes, J. Phys. Chem. Solid. 74 (2013) 599–604, https://doi.org/10.1016/j.jpcs.2012.12.013.

[37] V. Mortet, I. Gregora, A. Taylor, N. Lambert, P. Ashcheulov, Z. Gedeonova, P. Hubik, New perspectives for heavily boron-doped diamond Raman spectrum analysis, Carbon 168 (2020) 319–327, https://doi.org/10.1016/j.carbon.2020.06.075.

[38] V.A. Sidorov, E.A. Ekimov, Superconductivity in diamond, Diam. Relat. Mater. 19 (2010) 351–357, https://doi.org/10.1016/j.diamond.2009.12.002.

[39] A. Merlen, J.G. Buijnsters, C. Pardanaud, A guide to and review of the use of multiwavelength Raman spectroscopy for characterizing defective aromatic carbon solids: from graphene to amorphous carbons, Coatings (2017) 7, https://doi.org/10.3390/coatings7100153.

[40] A.F. Sartori, S. Orlando, A. Bellucci, D.M. Trucchi, S. Abrahami, T. Boehme, T. Hantschel, W. Vandervorst, J.G. Buijnsters, Laser-induced periodic surface structures (LIPSS) on heavily boron-doped diamond for electrode applications, ACS Appl. Mater. Interfaces 10 (2018) 43236–43251, https://doi.org/10.1021/acsami.8b15951.

[41] S.J. Cobb, F.H.J. Laidlaw, G. West, G. Wood, M.E. Newton, R. Beanland, J. V. Macpherson, Assessment of acid and thermal oxidation treatments for removing sp2 bonded carbon from the surface of boron doped diamond, Carbon 167 (2020) 1–10, https://doi.org/10.1016/j.carbon.2020.04.095.

[42] Raman analysis tool. http://ofm.fzu.cz/cs/raman-tool. (Accessed 15 September 2022).

[43] M. Brycht, S. Baluchova, A. Taylor, V. Mortet, S. Sedlakova, L. Klimsa, J. Kopecek, K. Schwarzova-Peckova, Comparison of electrochemical performance of various boron-doped diamond electrodes: dopamine sensing in biomimicking media used for cell cultivation, Bioelechrochemistry 137 (2021), https://doi.org/10.1016/j.bioelechem.2020.107646.

[44] P. Kuang, K. Natsui, C. Feng, Y. Einaga, Electrochemical reduction of nitrate on boron-doped diamond electrodes: effects of surface termination and boron-doping level, Chemosphere 251 (2020), 126364, https://doi.org/10.1016/j.chemosphere.2020.126364.

[45] H.B. Suffredini, S.A.S. Machado, L.A. Avaca, The water decomposition reactions on boron-doped diamond electrodes, J. Braz. Chem. Soc. 15 (2004) 16–21, https://doi.org/10.1590/s0103-50532004000100004.

[46] K. Schwarzová-Pecková, J. Vosáhlová, J. Barek, I. Šloufová, E. Pavlova, V. Petrák, J. Zavázalová, Influence of boron content on the morphological, spectral, and electroanalytical characteristics of anodically oxidized boron-doped diamond electrodes, Electrochim. Acta 243 (2017) 170–182, https://doi.org/10.1016/j.electacta.2017.05.006.

[47] I. Duo, A. Fujishima, C.H. Comninellis, Electron transfer kinetics on composite diamond (sp(3))-graphite (sp(2)) electrodes, Electrochem. Commun. 5 (2003) 695–700, https://doi.org/10.1016/s1388-2481(03)00169-3.

[48] Z.V. Živcová, V. Petrák, O. Frank, L. Kavan, Electrochemical impedance spectroscopy of polycrystalline boron doped diamond layers with hydrogen and oxygen terminated surface, Diam. Relat. Mater. 55 (2015) 70–76, https://doi.org/10.1016/j.diamond.2015.03.002.

[49] M.C. Granger, G.M. Swain, The influence of surface interactions on the reversibility of ferri/ferrocyanide at boron-doped diamond thin-film electrodes, J. Electrochem. Soc. 146 (1999) 4551–4558, https://doi.org/10.1149/1.1392673.

[50] I. Yagi, H. Notsu, T. Kondo, D.A. Tryk, A. Fujishima, Electrochemical selectivity for redox systems at oxygen-terminated diamond electrodes, J. Electroanal. Chem. 473 (1999) 173–178, https://doi.org/10.1016/S0022-0728(99)00027-3.

[51] M.C. Granger, M. Witek, J.S. Xu, J. Wang, M. Hupert, A. Hanks, M.D. Koppang, J. E. Butler, G. Lucazeau, M. Mermoux, J.W. Strojek, G.M. Swain, Standard electrochemical behavior of high-quality, boron-doped polycrystalline diamond thin-film electrodes, Anal. Chem. 72 (2000) 3793–3804, https://doi.org/10.1021/ac0000675.

[52] J.A. Bennett, J. Wang, Y. Show, G.M. Swain, Effect of sp2-bonded nondiamond carbon impurity on the response of boron-doped polycrystalline diamond thin-film electrodes, J. Electrochem. Soc. 151 (2004) E306, https://doi.org/10.1149/1.1780111.

[53] Y. Einaga, J.S. Foord, G.M. Swain, Diamond electrodes: diversity and maturity, MRS Bull. 39 (2014) 525–532, https://doi.org/10.1557/mrs.2014.94.

[54] T. Ando, K. Asai, J. Macpherson, Y. Einaga, T. Fukuma, Y. Takahashi, Nanoscale reactivity mapping of a single-crystal boron-doped diamond particle, Anal. Chem. 93 (2021) 5831–5838, https://doi.org/10.1021/acs.analchem.1c00053.

[55] A.N. Patel, S.-y. Tan, T.S. Miller, J.V. Macpherson, P.R. Unwin, Comparison and reappraisal of carbon electrodes for the voltammetric detection of dopamine, Anal. Chem. 85 (2013) 11755–11764, https://doi.org/10.1021/ac401969q.

[56] T. Watanabe, Y. Honda, K. Kanda, Y. Einaga, Tailored design of boron-doped diamond electrodes for various electrochemical applications with boron-doping level and sp2-bonded carbon impurities, Phys. Status Solidi 211 (2014) 2709–2717, https://doi.org/10.1002/pssa.201431455.

[57] R. Trouillon, Y. Einaga, M.A.M. Gijs, Cathodic pretreatment improves the resistance of boron-doped diamond electrodes to dopamine fouling, Electrochem. Commun. 47 (2014) 92–95, https://doi.org/10.1016/j.elecom.2014.07.028.

[58] L.Y. Jiang, G.W. Nelson, J. Abda, J.S. Foord, Novel modifications to carbon-based electrodes to improve the electrochemical detection of dopamine, ACS Appl. Mater. Interfaces 8 (2016) 28338–28348, https://doi.org/10.1021/acsami.6b03879.

[59] P.S. Siew, K.P. Loh, W.C. Poh, H. Zhang, Biosensing properties of nanocrystalline diamond film grown on polycrystalline diamond electrodes, Diam. Relat. Mater. 14 (2005) 426–431, https://doi.org/10.1016/j.diamond.2004.11.016.

[60] S. Baluchová, A. Taylor, V. Mortet, S. Sedláková, L. Klimša, J. Kopeček, O. Hák, K. Schwarzová-Pecková, Porous boron doped diamond for dopamine sensing: effect of boron doping level on morphology and electrochemical performance, Electrochim. Acta 327 (2019), 135025, https://doi.org/10.1016/j.electacta.2019.135025.

[61] M. Wei, Z.Y. Xie, L.G. Sun, Z.Z. Gu, Electrochemical properties of a boron-doped diamond electrode modified with gold/polyelectrolyte hollow spheres, Electroanalysis 21 (2009) 138–143, https://doi.org/10.1002/elan.200804411.

[62] M. Wei, C. Terashima, M. Lv, A. Fujishima, Z.Z. Gu, Boron-doped diamond nanograss array for electrochemical sensors, Chem. Commun. (2009) 3624–3626, https://doi.org/10.1039/b903284c.

[63] Z. Deng, R. Zhu, L. Ma, K. Zhou, Z. Yu, Q. Wei, Diamond for antifouling applications: a review, Carbon 196 (2022) 923–939, https://doi.org/10.1016/j.carbon.2022.05.015.

[64] I. Shpilevaya, J.S. Foord, Electrochemistry of methyl viologen and anthraquinonedisulfonate at diamond and diamond powder electrodes: the influence of surface chemistry, Electroanalysis 26 (2014) 2088–2099, https://doi.org/10.1002/elan.201400310.

[65] J. Xu, Q. Chen, G.M. Swain, Anthraquinonedisulfonate electrochemistry: a comparison of glassy carbon, hydrogenated glassy carbon, highly oriented pyrolytic graphite, and diamond electrodes, Anal. Chem. 70 (1998) 3146–3154, https://doi.org/10.1021/ac9800661.